APPLIED MATHEMATICS AND MECHANICS (ENGLISH EDITION)

Parametric resonance of axially functionally graded pipes conveying pulsating fluid[*]

Jie JING[1], Xiaoye MAO[1,2,†], Hu DING[1,2], Liqun CHEN[1,2]

1. Shanghai Key Laboratory of Mechanics in Energy Engineering, Shanghai Frontier Science Center of Mechanoinformatics, Shanghai Institute of Applied Mathematics and Mechanics, School of Mechanics and Engineering Science, Shanghai University, Shanghai 200444, China;

2. Shanghai Institute of Aircraft Mechanics and Control, Shanghai 200092, China

Abstract Based on the generalized Hamilton's principle, the nonlinear governing equation of an axially functionally graded (AFG) pipe is established. The non-trivial equilibrium configuration is superposed by the modal functions of a simply supported beam. Via the direct multi-scale method, the response and stability boundary to the pulsating fluid velocity are solved analytically and verified by the differential quadrature element method (DQEM). The influence of Young's modulus gradient on the parametric resonance is investigated in the subcritical and supercritical regions. In general, the pipe in the supercritical region is more sensitive to the pulsating excitation. The nonlinearity changes from hard to soft, and the non-trivial equilibrium configuration introduces more frequency components to the vibration. Besides, the increasing Young's modulus gradient improves the critical pulsating flow velocity of the parametric resonance, and further enhances the stability of the system. In addition, when the temperature increases along the axial direction, reducing the gradient parameter can enhance the response asymmetry. This work further complements the theoretical analysis of pipes conveying pulsating fluid.

Key words pipe conveying fluid, axially functionally graded, supercritical resonance, multi-scale method, parametric resonance

Chinese Library Classification O322
2010 Mathematics Subject Classification 34A34, 70K50

1 Introduction

Pipes are widely used in aircraft and other engineering machinery[1–6]. Throughout their service life, vibration always causes fatigue, oil leaking, and even catastrophic incidents. Relevant research has shown that the pulsating velocity has an important effect on the vibration and

stability of the pipe. Therefore, the research on the parametric resonance of pipes conveying fluid caused by the pulsating velocity is now an important topic.

The vibration problem of pipes conveying fluid has been widely studied. Païdoussis and Issid[7] and Plaut and Huseyin[8] are pioneers. Matsuzaki and Fung[9] introduced geometric nonlinearity into the governing equation. Panda and Kar[10] studied the nonlinear dynamics of a simply supported pipe conveying pulsating fluid. Burak-Özhan and Pakdemirli[11] studied the principal parametric resonance of viscoelastic pipes conveying fluid with cubic nonlinearity. Zhu et al.[12] found that the steady-state response became asymmetric when an inclined simply supported pipe was subjected to nonlinear forced and parametric excitation. Shaik et al.[13] studied the parametric instability of high-pressure pipes conveying pulsating fluid, emphasizing the influence of the average velocity. Wei et al.[14] found that the nonlinear support stiffness affected the parametric vibration amplitude. Guo et al.[15] proposed a modified transfer matrix model to analyze the vibration of a pipe under base excitation and pulsating excitation. Wang et al.[16] observed abundant dynamic behaviors for cantilevered pipes conveying pulsating fluid. Guo et al.[17] and Zhu et al.[18] found that the dynamic behaviors of pipes in subcritical and supercritical regions were different. The dynamic behaviors such as periodic, period-doubling, and chaotic motions would appear in the supercritical region[19–25]. Therefore, it is necessary to study the parametric resonance of pipes in subcritical and supercritical regions.

Compared with homogeneous materials, functionally graded materials (FGMs) are more resistant to environmental gradients, such as temperature and humidity. Therefore, FGMs have been increasingly utilized in engineering structures[26–28]. Extensive research has been conducted on the nonlinear vibration characteristics of FGM pipes when the material parameters change along the radial direction[29–31]. Jin et al.[32] studied the nonlinear response of FGM nanotubes under combined forced and parametric excitation. Ding et al.[33] investigated the nonlinear buckled and primary resonance of FGM pipes. However, the pipe conveying fluid near an aero-engine or rocket engine is always subjected to temperature[34–36], which makes Young's modulus of the pipe change along the axial gradient. Such pipes are called axial functionally graded (AFG) pipes, which are more complicated than homogeneous pipes. The study on AFG pipe dynamics is a challenging topic.

The nonlinear vibration of AFG pipes has been widely studied. An and Su[37] established a model for an AFG pipe, and analyzed the vibration and stability of the pipe. Lu et al.[38] analyzed the internal resonance and fatigue properties of an AFG pipe under parametric excitation so as to improve the fatigue life. Guo et al.[39] proposed an effective method to analyze the random natural frequency of AFG pipes. Tuo et al.[40] found that the increase in Young's modulus ratio could reduce the natural frequency of AFG pipes. Fan et al.[41] investigated the influence of fluid velocity, volume fraction, and fluid density on the resonance reliability of AFG pipes. Aghazadeh[42–43] proposed a new stability and dynamic analysis model of AFG pipes, and found that the dynamic response of AFG pipes could be adjusted by selecting appropriate parameters. Fu et al.[44] studied the nonlinear dynamics of an AFG pipe conveying pulsating fluid, and found that the material properties caused the pipe to undergo chaotic, periodic, and quasi-periodic motion transitions. However, most of the afore-mentioned research focuses on the subcritical region, and lacks quantitative analyses on the parametric vibration of AFG pipes. Therefore, it is of academic value to supplement a parametric vibration analysis on AFG pipes in the supercritical region.

In this paper, based on the AFG pipe model with simply supported boundaries, the influence of pulsating fluid in the pipe is considered. Based on the generalized Hamilton's principle, the parametric vibration governing equation of the AFG pipe in the supercritical region is established. The solvability condition for the parametric vibration of the AFG pipe is presented, the stability is analyzed, and the amplitude-frequency responses are achieved. The correctness of the approximate analytical results is verified by the differential quadrature element method (DQEM). The effects of pulsating velocity and Young's modulus gradient on the parametric

vibration of the AFG pipe are discussed, and the response asymmetry is analyzed. Finally, the response characteristics before and after buckling are compared, and the influence of Young's modulus gradient on the parametric resonance is obtained. The development of the pipe is further complemented.

2   Mathematical model

The diagram in Fig. 1 illustrates a physical model of an AFG pipe conveying fluid, which is supported at both ends. The axial and radial coordinates are denoted by x and y, respectively. The lateral displacement of the pipe is represented by $v(x,t)$, while the longitudinal displacement is denoted as $u(x,t)$. The length of the pipe is denoted as L. D and d refer to the outer and inner diameters of the pipe, respectively. I_{p} represents the moment of inertia for its cross section. P_0 denotes the initial axial force acting on the pipe.
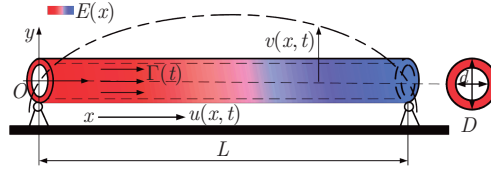

Fig. 1   Model of the AFG pipe conveying fluid (color online)

$E(x)$ and $\rho_{\mathrm{p}}(x)$ represent Young's modulus and the density of the pipe changing along the axial direction, respectively[38,45], and

$$E(x) = E_0\Big(1 + \frac{x}{L}(\alpha_E - 1)\Big), \quad \rho_{\mathrm{p}}(x) = \rho_0\Big(1 + \frac{x}{L}(\alpha_\rho - 1)\Big), \tag{1}$$

where α_E and α_ρ are the gradient parameters of Young's modulus and the density, respectively. Considering the effect of unsteady flow, the density of the fluid is ρ_{f}. Suppose that the velocity of the fluid in the pipe pulsates periodically near the average velocity as

$$\Gamma = \Gamma_0 + \Gamma_1 \sin(\Omega_{\mathrm{p}}t), \tag{2}$$

where Γ_0 is the average velocity, Γ_1 is the pulsating amplitude, and Ω_{p} is the pulsating frequency, E_0 is Young's modulus, and ρ_0 is the pipe density. The change of flow velocity will cause parametric vibration, but the longitudinal displacement is small enough to be ignored. Based on the Euler-Bernoulli beam theory and the generalized Hamilton's principle, the transverse vibration model of the subcritical AFG pipe conveying pulsating fluid is established[46]. The governing equation is

$$\Big(\rho_0 A_{\mathrm{p}}\Big(1 + \frac{x}{L}(\alpha_\rho - 1)\Big) + \rho_{\mathrm{f}} A_{\mathrm{f}}\Big)v_{,tt} + 2\rho_{\mathrm{f}} A_{\mathrm{f}}(\Gamma_0 + \Gamma_1 \sin(\Omega_{\mathrm{p}}t))v_{,xt} + (\rho_{\mathrm{f}} A_{\mathrm{f}}\Gamma_0^2 - P_0)v_{,xx}$$

$$+ \rho_{\mathrm{f}} A_{\mathrm{f}}(\Gamma_1^2 \sin^2(\Omega_{\mathrm{p}}t) + 2\Gamma_0\Gamma_1 \sin(\Omega_{\mathrm{p}}t))v_{,xx} + \rho_{\mathrm{f}} A_{\mathrm{f}}\Gamma_1\Omega_{\mathrm{p}}\cos(\Omega_{\mathrm{p}}t)v_{,x} + \frac{2E_0 I_{\mathrm{p}}(\alpha_E - 1)}{L}v_{,xxx}$$

$$+ E_0 I_{\mathrm{p}}\Big(1 + \frac{x}{L}(\alpha_E - 1)\Big)v_{,xxxx} - \frac{E_0 A_{\mathrm{p}}(\alpha_E - 1)}{2L\ln(\alpha_E)}v_{,xx}\int_0^L v_{,x}^2\mathrm{d}x + \frac{2\mu I_{\mathrm{p}}(\alpha_E - 1)}{L}v_{,xxxt}$$

$$+ \mu I_{\mathrm{p}}\Big(1 + \frac{x}{L}(\alpha_E - 1)\Big)v_{,xxxxt} - \frac{\mu A_{\mathrm{p}}(\alpha_E - 1)}{2L\ln(\beta_\mu)}\Big(v_{,xxt}\int_0^L v_{,x}^2\mathrm{d}x + 2v_{,xx}\int_0^L v_{,x}v_{,xt}\mathrm{d}x\Big) = 0, \tag{3}$$

where the comma preceding x or t denotes partial differentiation with respect to x or t. The simply supported boundary conditions are

$$v(0,t) = 0, \quad v(L,t) = 0, \quad v_{,xx}(0,t) = 0, \quad v_{,xx}(L,t) = 0. \tag{4}$$

Based on the previous research, the non-trivial equilibrium configuration is considered as the fundamental basis for investigating the vibration characteristics of a supercritical AFG pipe conveying fluid. By neglecting the terms involving time in Eq. (3), the static governing equation and the corresponding boundary conditions are obtained as follows:

$$(\rho_{\mathrm{f}} A_{\mathrm{f}} \Gamma_0^2 - P_0) \widehat{v}_{,xx} + \frac{2E_0 I_{\mathrm{p}}(\alpha_E - 1)}{L} \widehat{v}_{,xxx} + E_0 I_{\mathrm{p}} \Big(1 + \frac{x}{L}(\alpha_E - 1)\Big) \widehat{v}_{,xxxx}$$

$$- \frac{E_0 A_{\mathrm{p}}(\alpha_E - 1)}{2L \ln(\alpha_E)} \widehat{v}_{,xx} \int_0^L \widehat{v}_{,x}^2 \mathrm{d}x = 0, \tag{5}$$

$$\widehat{v}(0) = 0, \quad \widehat{v}(L) = 0, \quad \widehat{v}_{,xx}(0) = 0, \quad \widehat{v}_{,xx}(L) = 0. \tag{6}$$

According to Ref. [46], the approximate analytical solution to Eq. (5) can be obtained. Therefore, the non-trivial static equilibrium configuration is

$$\widehat{v}(x) = \sum_{i=1}^{n} B_i \sin\Big(\frac{i\pi x}{L}\Big), \tag{7}$$

where $B_1, B_2, \cdots, B_n$ are the configuration coefficients. The AFG pipe vibrates around the new equilibrium configuration in the supercritical region, and thus the transverse vibration is divided into two parts. Make the following coordinate transformation:

$$v(x,t) \to v(x,t) + \widehat{v}(x)^+. \tag{8}$$

Since the non-trivial equilibrium configuration is symmetrical across the x-axial, only the positive non-trivial equilibrium configuration $\widehat{v}(x)^+$ is considered. Substituting Eq. (8) into Eq. (3) and combining Eq. (5) yield the governing equation of the supercritical AFG pipe conveying pulsating fluid as follows:

$$\Big(\rho_0 A_{\mathrm{p}} \Big(1 + \frac{x}{L}(\alpha_\rho - 1)\Big) + \rho_{\mathrm{f}} A_{\mathrm{f}}\Big) v_{,tt} + 2\rho_{\mathrm{f}} A_{\mathrm{f}} (\Gamma_0 + \Gamma_1 \sin(\Omega_{\mathrm{p}} t)) v_{,xt}$$

$$+ (\rho_{\mathrm{f}} A_{\mathrm{f}} \Gamma_0^2 - P_0) v_{,xx} + \rho_{\mathrm{f}} A_{\mathrm{f}} (\Gamma_1^2 \sin^2(\Omega_{\mathrm{p}} t) + 2\Gamma_0 \Gamma_1 \sin(\Omega_{\mathrm{p}} t))(v_{,xx} + \widehat{v}_{,xx}^+)$$

$$+ \rho_{\mathrm{f}} A_{\mathrm{f}} \Gamma_1 \Omega_{\mathrm{p}} \cos(\Omega_{\mathrm{p}} t)(v_{,x} + \widehat{v}_{,x}^+) + \frac{2E_0 I_{\mathrm{p}}(\alpha_E - 1)}{L} v_{,xxx} + E_0 I_{\mathrm{p}} \Big(1 + \frac{x}{L}(\alpha_E - 1)\Big) v_{,xxxx}$$

$$- \frac{E_0 A_{\mathrm{p}}(\alpha_E - 1)}{2L \ln(\alpha_E)} v_{,xx} \int_0^L (v_{,x} + \widehat{v}_{,x}^+)^2 \mathrm{d}x - \frac{E_0 A_{\mathrm{p}}(\alpha_E - 1)}{2L \ln(\alpha_E)} \widehat{v}_{,xx}^+ \int_0^L (v_{,x}^2 + 2v_{,x} \widehat{v}_{,x}^+) \mathrm{d}x$$

$$+ \frac{2\mu I_{\mathrm{p}}(\beta_\mu - 1)}{L} v_{,xxxt} + \mu I_{\mathrm{p}} \Big(1 + \frac{x}{L}(\beta_\mu - 1)\Big) v_{,xxxxt} - \frac{\mu A_{\mathrm{p}}(\beta_\mu - 1)}{2L \ln(\beta_\mu)} v_{,xxt} \int_0^L (v_{,x} + \widehat{v}_{,x}^+)^2 \mathrm{d}x$$

$$- \frac{\mu A_{\mathrm{p}}(\beta_\mu - 1)}{L \ln(\beta_\mu)} (v_{,xx} + \widehat{v}_{,xx}^+) \int_0^L (v_{,x} + \widehat{v}_{,x}^+) v_{,xt} \mathrm{d}x = 0, \tag{9}$$

where μ is the viscous damping coefficient.

Unless otherwise stated, the model parameters are selected as follows:

$$\begin{cases} D = 0.02\,\mathrm{m}, \quad d = 0.018\,\mathrm{m}, \quad E_0 = 176.36\,\mathrm{GPa}, \quad P_0 = 20\,\mathrm{N}, \quad \mu = 2 \times 10^6\,\mathrm{N \cdot s \cdot m^{-2}}, \\ \rho_0 = 7\,209.09\,\mathrm{kg \cdot m^{-3}}, \quad \rho_{\mathrm{f}} = 872\,\mathrm{kg \cdot m^{-3}}, \quad L = 1\,\mathrm{m}, \quad \alpha_E = \alpha_\rho = \beta_\mu = 1.2. \end{cases}$$

According to Ref. [46] and the above-mentioned parameters, under different Young's modulus gradients, the relationship between the natural frequency and the average flow velocity of the pipe before and after buckling is shown in Table 1, in which $\Gamma_{0\text{-cr}}$ is the critical flow velocity, and $\Gamma_{0\text{-sub}}$ and $\Gamma_{0\text{-sup}}$ are the subcritical and supercritical flow velocities, respectively.

Table 1 Comparison of values before and after buckling ($\Gamma_{0\text{-sup}} = 1.1\Gamma_{0\text{-cr}}$)

α_E	$\Gamma_{0\text{-sub}}/(\text{m·s}^{-1})$	$\Gamma_{0\text{-cr}}/(\text{m·s}^{-1})$	$\Gamma_{0\text{-sup}}/(\text{m·s}^{-1})$	$\omega_1/(\text{rad·s}^{-1})$
0.4	93.69	120.12	132.13	131.00
0.6	100.76	129.82	142.80	142.38
0.8	107.20	138.27	152.10	151.79
1	113.07	145.87	160.46	160.20
1.2	118.47	152.85	168.14	167.95
1.4	123.50	159.35	175.29	175.20
1.6	128.27	165.46	182.01	181.97

3   Method introduction

3.1   Direct multi-scale method

The multi-scale method is a classical method for analyzing nonlinear vibration, which is applicable to periodic or dissipative motions of discrete or continuous systems. Considering the cubic nonlinearity in the equation, the following time scales are introduced:

$$T_0 = t, \quad T_1 = \varepsilon t, \quad T_2 = \varepsilon^2 t, \tag{10}$$

where ε represents a negligible value. T_0 represents the fast time scale of the linear system excluding viscoelastic damping and external excitation, T_1 denotes a slower time scale, and T_2 denotes an even slower time scale. Assume the solution to Eq. (9) as follows:

$$v(x,t) = v_0(x, T_0, T_1, T_2) + \varepsilon v_1(x, T_0, T_1, T_2) + \varepsilon^2 v_2(x, T_0, T_1, T_2). \tag{11}$$

To make the damping and external excitation appear in the same equation with the highest order nonlinear terms, the relevant parameters are rescaled as follows:

$$v(x,t) = \varepsilon v(x,t), \quad \mu = \varepsilon^2 \mu, \quad \Gamma_1 = \varepsilon^2 \Gamma_1. \tag{12}$$

Some time scale differential operators can be defined by

$$\begin{cases} \dfrac{\mathrm{d}}{\mathrm{d}t} = \mathrm{D}_0 + \varepsilon \mathrm{D}_1 + \varepsilon^2 \mathrm{D}_2 + \cdots, \\[2mm] \dfrac{\mathrm{d}^2}{\mathrm{d}t^2} = \mathrm{D}_0^2 + 2\varepsilon \mathrm{D}_0 \mathrm{D}_1 + \varepsilon^2 (\mathrm{D}_1^2 + 2\mathrm{D}_0 \mathrm{D}_2) + \cdots, \\[2mm] \mathrm{D}_k = \dfrac{\partial(\cdot)}{\partial T_k}. \end{cases} \tag{13}$$

Substituting Eqs. (10)–(13) into Eq. (9), neglecting higher order small quantities over the third order, and then separating the homogeneous power terms yield the T_0 scale equation

$$\left(\rho_0 A_\mathrm{p} \left(1 + \frac{x}{L}(\alpha_\rho - 1) \right) + \rho_\mathrm{f} A_\mathrm{f} \right) \mathrm{D}_0^2 v_0 + 2\rho_\mathrm{f} A_\mathrm{f} \Gamma_0 \mathrm{D}_0 v_{0,x}$$

$$+ (\rho_\mathrm{f} A_\mathrm{f} \Gamma_0^2 - P_0) v_{0,xx} + \frac{2E_0 I_\mathrm{p}(\alpha_E - 1)}{L} v_{0,xxx} + E_0 I_\mathrm{p} \left(1 + \frac{x}{L}(\alpha_E - 1) \right) v_{0,xxxx}$$

$$- \frac{E_0 A_\mathrm{p}(\alpha_E - 1)}{2L \ln(\alpha_E)} v_{0,xx} \int_0^L (\widehat{v}_{,x}^+)^2 \mathrm{d}x - \frac{E_0 A_\mathrm{p}(\alpha_E - 1)}{L \ln(\alpha_E)} \widehat{v}_{,xx}^+ \int_0^L v_{0,x} \widehat{v}_{,x}^+ \mathrm{d}x = 0 \tag{14}$$

with the boundary conditions

$$v_0(0) = 0, \quad v_0(L) = 0, \quad v_{0,xx}(0) = 0, \quad v_{0,xx}(L) = 0, \tag{15}$$

the T_1 scale equation

$$\left(\rho_0 A_{\mathrm{p}}\left(1 + \frac{x}{L}(\alpha_\rho - 1)\right) + \rho_{\mathrm{f}} A_{\mathrm{f}}\right)\mathrm{D}_0^2 v_1 + 2\left(\rho_0 A_{\mathrm{p}}\left(1 + \frac{x}{L}(\alpha_\rho - 1)\right) + \rho_{\mathrm{f}} A_{\mathrm{f}}\right)\mathrm{D}_0\mathrm{D}_1 v_0$$

$$+ 2\rho_{\mathrm{f}} A_{\mathrm{f}} \Gamma_0 (\mathrm{D}_0 v_{1,x} + \mathrm{D}_1 v_{0,x}) + (\rho_{\mathrm{f}} A_{\mathrm{f}} \Gamma_0^2 - P_0) v_{1,xx} + \frac{2E_0 I_{\mathrm{p}}(\alpha_E - 1)}{L} v_{1,xxx}$$

$$+ E_0 I_{\mathrm{p}}\left(1 + \frac{x}{L}(\alpha_E - 1)\right) v_{1,xxxx} + 2\rho_{\mathrm{f}} A_{\mathrm{f}} \Gamma_0 \Gamma_1 \sin(\Omega_{\mathrm{p}} T_0) \widehat{v}_{,xx}^+$$

$$+ \rho_{\mathrm{f}} A_{\mathrm{f}} \Gamma_1 \Omega_{\mathrm{p}} \cos(\Omega_{\mathrm{p}} T_0) \widehat{v}_{,x}^+ - \frac{E_0 A_{\mathrm{p}}(\alpha_E - 1)}{L \ln(\alpha_E)} v_{0,xx} \int_0^L \widehat{v}_{,x}^+ v_{0,x} \mathrm{d}x$$

$$- \frac{E_0 A_{\mathrm{p}}(\alpha_E - 1)}{2L \ln(\alpha_E)} v_{1,xx} \int_0^L (\widehat{v}_{,x}^+)^2 \mathrm{d}x - \frac{E_0 A_{\mathrm{p}}(\alpha_E - 1)}{2L \ln(\alpha_E)} \widehat{v}_{,xx}^+ \int_0^L (v_{0,x}^2 + 2\widehat{v}_{,x}^+ v_{1,x}) \mathrm{d}x = 0 \quad (16)$$

with the boundary conditions

$$v_1(0) = v_1(L) = 0, \quad v_{1,xx}(0) = v_{1,xx}(L) = 0, \quad (17)$$

and the T_2 scale equation

$$2\left(\rho_0 A_{\mathrm{p}}\left(1 + \frac{x}{L}(\alpha_\rho - 1)\right) + \rho_{\mathrm{f}} A_{\mathrm{f}}\right)(\mathrm{D}_0\mathrm{D}_1 v_1 + \mathrm{D}_0\mathrm{D}_2 v_0) + 2\rho_{\mathrm{f}} A_{\mathrm{f}} \Gamma_1 \sin(\Omega_{\mathrm{p}} T_0)\mathrm{D}_0 v_{0,x}$$

$$+ \left(\rho_0 A_{\mathrm{p}}\left(1 + \frac{x}{L}(\alpha_\rho - 1)\right) + \rho_{\mathrm{f}} A_{\mathrm{f}}\right)(\mathrm{D}_0^2 v_2 + \mathrm{D}_1^2 v_0) + (\rho_{\mathrm{f}} A_{\mathrm{f}} \Gamma_0^2 - P_0) v_{2,xx}$$

$$+ 2\rho_{\mathrm{f}} A_{\mathrm{f}} \Gamma_0 (\mathrm{D}_0 v_{2,x} + \mathrm{D}_1 v_{1,x} + \mathrm{D}_2 v_{0,x}) + 2\rho_{\mathrm{f}} A_{\mathrm{f}} \Gamma_0 \Gamma_1 \sin(\Omega_{\mathrm{p}} T_0) v_{0,xx}$$

$$+ \rho_{\mathrm{f}} A_{\mathrm{f}} \Gamma_1 \Omega_{\mathrm{p}} \cos(\Omega_{\mathrm{p}} T_0) v_{0,x} + \frac{2E_0 I_{\mathrm{p}}(\alpha_E - 1)}{L} v_{2,xxx} + E_0 I_{\mathrm{p}}\left(1 + \frac{x}{L}(\alpha_E - 1)\right) v_{2,xxxx}$$

$$+ \frac{2\mu I_{\mathrm{p}}(\beta_\mu - 1)}{L}\mathrm{D}_0 v_{0,xxx} + \mu I_{\mathrm{p}}\left(1 + \frac{x}{L}(\beta_\mu - 1)\right)\mathrm{D}_0 v_{0,xxxx} - \frac{\mu A_{\mathrm{p}}(\beta_\mu - 1)}{2L \ln(\alpha_E)}\mathrm{D}_0 v_{0,xx} \int_0^L (\widehat{v}_{,x}^+)^2 \mathrm{d}x$$

$$- \frac{\mu A_{\mathrm{p}}(\beta_\mu - 1)}{L \ln(\alpha_E)} \widehat{v}_{,xx}^+ \int_0^L \widehat{v}_{,x}^+ \mathrm{D}_0 v_{0,x} \mathrm{d}x - \frac{E_0 A_{\mathrm{p}}(\alpha_E - 1)}{2L \ln(\alpha_E)} v_{2,xx} \int_0^L (\widehat{v}_{,x}^+)^2 \mathrm{d}x$$

$$- \frac{E_0 A_{\mathrm{p}}(\alpha_E - 1)}{L \ln(\alpha_E)} v_{1,xx} \int_0^L \widehat{v}_{,x}^+ v_{0,x} \mathrm{d}x - \frac{E_0 A_{\mathrm{p}}(\alpha_E - 1)}{2L \ln(\alpha_E)} v_{0,xx} \int_0^L (v_{0,x}^2 + 2\widehat{v}_{,x}^+ v_{1,x}) \mathrm{d}x$$

$$- \frac{E_0 A_{\mathrm{p}}(\alpha_E - 1)}{L \ln(\alpha_E)} \widehat{v}_{,xx}^+ \int_0^L (\widehat{v}_{,x}^+ v_{2,x} + v_{0,x} v_{1,x}) \mathrm{d}x = 0 \quad (18)$$

with the boundary conditions

$$v_2(0) = v_2(L) = 0, \quad v_{2,xx}(0) = v_{2,xx}(L) = 0. \quad (19)$$

After rescaling, the original nonlinear system is transformed into a linear problem on different time scales, which needs to be solved layer by layer. Assume that the solution to Eq. (14) is

$$v_0(x, T_0, T_1, T_2) = A_1(T_1, T_2)\Phi_1(x)\mathrm{e}^{\mathrm{i}\omega_1 T_0} + \mathrm{c.c.}, \quad (20)$$

where A_1 is the undetermined response function. $\Phi_1(x)$ and ω_1 are the first-order modal function and the first-order natural frequency of the linear derived system, respectively. c.c. denotes the complex conjugate of the previous exponential terms, which will not be repeated later. To obtain a relatively accurate solution, the modal function contains the first two modes[47]. Therefore, the modal function and its conjugate can be expressed as

$$\Phi_1(x) = \sum_{k=1}^2 p_{1,k} \sin\left(\frac{k\pi x}{L}\right), \quad \overline{\Phi}_1(x) = \sum_{k=1}^2 \overline{p}_{1,k} \sin\left(\frac{k\pi x}{L}\right), \quad (21)$$

where $p_{1,k}$ are undetermined coefficients, which can be obtained by the method of undetermined coefficients (see Appendix A).

Substituting Eq. (20) into Eq. (16) yields

$$
\begin{aligned}
&\left(\rho_0 A_\mathrm{p}\left(1 + \frac{x}{L}(\alpha_\rho - 1)\right) + \rho_\mathrm{f} A_\mathrm{f}\right) \mathrm{D}_0^2 v_1 + 2\rho_\mathrm{f} A_\mathrm{f} \Gamma_0 \mathrm{D}_0 v_{1,x} + (\rho_\mathrm{f} A_\mathrm{f} \Gamma_0^2 - P_0) v_{1,xx} \\
&+ \frac{2E_0 I_\mathrm{p}(\alpha_E - 1)}{L} v_{1,xxx} + E_0 I_\mathrm{p}\left(1 + \frac{x}{L}(\alpha_E - 1)\right) v_{1,xxxx} - \frac{E_0 A_\mathrm{p}(\alpha_E - 1)}{2L \ln(\alpha_E)} v_{1,xx} \int_0^L (\widehat{v}_{,x}^+)^2 \mathrm{d}x \\
&- \frac{E_0 A_\mathrm{p}(\alpha_E - 1)}{L \ln(\alpha_E)} \widehat{v}_{,xx}^+ \int_0^L \widehat{v}_{,x}^+ v_{1,x} \mathrm{d}x + 2\rho_\mathrm{f} A_\mathrm{f} \Gamma_0 \Gamma_1 \sin(\Omega_\mathrm{p} T_0) \widehat{v}_{,xx}^+ + \rho_\mathrm{f} A_\mathrm{f} \Gamma_1 \Omega_\mathrm{p} \cos(\Omega_\mathrm{p} T_0) \widehat{v}_{,x}^+ \\
&- \frac{E_0 A_\mathrm{p}(\alpha_E - 1)}{2L \ln(\alpha_E)} \widehat{v}_{,xx}^+ \int_0^L A_1(T_1, T_2) \overline{A}_1(T_1, T_2) \frac{\mathrm{d}\Phi_1(x)}{\mathrm{d}x} \frac{\mathrm{d}\overline{\Phi}_1(x)}{\mathrm{d}x} \mathrm{d}x \\
&- \frac{E_0 A_\mathrm{p}(\alpha_E - 1)}{2L \ln(\alpha_E)} \widehat{v}_{,xx}^+ \int_0^L A_1(T_1, T_2)^2 \left(\frac{\mathrm{d}\Phi_1(x)}{\mathrm{d}x}\right)^2 \mathrm{e}^{2\mathrm{i}\omega_1 T_0} \mathrm{d}x \\
&- \frac{E_0 A_\mathrm{p}(\alpha_E - 1)}{L \ln(\alpha_E)} A_1(T_1, T_2) \overline{A}_1(T_1, T_2) \frac{\mathrm{d}^2\overline{\Phi}_1(x)}{\mathrm{d}x^2} \int_0^L \widehat{v}_{,x}^+ \frac{\mathrm{d}\Phi_1(x)}{\mathrm{d}x} \mathrm{d}x \\
&- \frac{E_0 A_\mathrm{p}(\alpha_E - 1)}{L \ln(\alpha_E)} A_1(T_1, T_2)^2 \frac{\mathrm{d}^2\Phi_1(x)}{\mathrm{d}x^2} \mathrm{e}^{2\mathrm{i}\omega_1 T_0} \int_0^L \widehat{v}_{,x}^+ \frac{\mathrm{d}\Phi_1(x)}{\mathrm{d}x} \mathrm{d}x \\
&+ 2\left(\rho_0 A_\mathrm{p}\left(1 + \frac{x}{L}(\alpha_\rho - 1)\right) + \rho_\mathrm{f} A_\mathrm{f}\right) \mathrm{D}_0 \mathrm{D}_1 A_1(T_1, T_2) \Phi_1(x) \mathrm{e}^{\mathrm{i}\omega_1 T_0} \\
&+ 2\rho_\mathrm{f} A_\mathrm{f} \Gamma_0 \mathrm{D}_1 A_1(T_1, T_2) \frac{\mathrm{d}\Phi_1(x)}{\mathrm{d}x} \mathrm{e}^{\mathrm{i}\omega_1 T_0} + \mathrm{c.c.} = 0.
\end{aligned}
\tag{22}
$$

Obviously, the last two exponential terms in Eq. (22) are the secular terms. In actual systems, secular terms do not exist. Therefore, A_1 is independent of the time scale T_1,

$$
A_1(T_1, T_2) = A_1(T_2), \quad \overline{A}_1(T_1, T_2) = \overline{A}_1(T_2),
\tag{23}
$$

where $\overline{A}_1(T_2)$ is the complex conjugate. According to Eq. (22), the special solution to Eq. (16) is assumed as

$$
v_1(x, T_0, T_2) = Z_1(x, T_2) \mathrm{e}^{2\mathrm{i}\omega_1 T_0} + Z_2(x, T_2) \mathrm{e}^{\mathrm{i}\Omega_\mathrm{p} T_0} + \mathrm{c.c.} + Z_3(x, T_2),
\tag{24}
$$

where the modal functions Z_i are expanded as

$$
\begin{cases}
Z_n(x, T_2) = \displaystyle\sum_{k=1}^{2} s_{n,k}(T_2) \sin\left(\frac{k\pi x}{L}\right), & n = 1, 2, 3, \\[2ex]
\overline{Z}_n(x, T_2) = \displaystyle\sum_{k=1}^{2} \overline{s}_{n,k}(T_2) \sin\left(\frac{k\pi x}{L}\right), & n = 1, 2.
\end{cases}
\tag{25}
$$

Similarly, the method of undetermined coefficients can be adopted to calculate the coefficients $s_{n,k}$ and their complex conjugates. To find the secular term, only the homogeneous solution to the T_2 scale equation needs to be considered,

$$
v_2(x, T_0, T_2) = Q_1(x, T_2) \mathrm{e}^{\mathrm{i}\omega_1 T_0},
\tag{26}
$$

where

$$
Q_1(x, T_2) = \sum_{k=1}^{2} q_{1,k}(T_2) \sin\left(\frac{k\pi x}{L}\right).
\tag{27}
$$

The pulsating frequency of the fluid is close to two times the natural frequency, and parametric resonance may occur in the system. A detuning parameter σ is introduced as follows:

$$\Omega_{\mathrm{p}} = 2\omega_1 + \varepsilon^2\sigma. \tag{28}$$

The following Euler's formulae are introduced:

$$\sin(\Omega_{\mathrm{p}}T_0) = \frac{1}{2}\mathrm{i}(\mathrm{e}^{-\mathrm{i}\Omega_{\mathrm{p}}T_0} - \mathrm{e}^{\mathrm{i}\Omega_{\mathrm{p}}T_0}), \quad \cos(\Omega_{\mathrm{p}}T_0) = \frac{1}{2}(\mathrm{e}^{-\mathrm{i}\Omega_{\mathrm{p}}T_0} + \mathrm{e}^{\mathrm{i}\Omega_{\mathrm{p}}T_0}). \tag{29}$$

Substitute Eqs. (20), (24), (26), and (28) into Eq. (18), and extract the coefficients of $\mathrm{e}^{\mathrm{i}\omega_1 T_0}$. Then, we have

$$
\begin{aligned}
&- \Big(\rho_0 A_{\mathrm{p}}\Big(1 + \frac{x}{L}(\alpha_\rho - 1)\Big) + \rho_{\mathrm{f}}A_{\mathrm{f}}\Big)\omega_1^2 Q_1(x, T_2) + 2\mathrm{i}\omega_1\rho_{\mathrm{f}}A_{\mathrm{f}}\Gamma_0\frac{\partial Q_1(x, T_2)}{\partial x} \\
&+ (\rho_{\mathrm{f}}A_{\mathrm{f}}\Gamma_0^2 - P_0)\frac{\partial^2 Q_1(x, T_2)}{\partial x^2} + \frac{2E_0 I_{\mathrm{p}}(\alpha_E - 1)}{L}\frac{\partial^3 Q_1(x, T_2)}{\partial x^3} \\
&+ E_0 I_{\mathrm{p}}\Big(1 + \frac{x}{L}(\alpha_E - 1)\Big)\frac{\partial^4 Q_1(x, T_2)}{\partial x^4} - \frac{E_0 A_{\mathrm{p}}(\alpha_E - 1)}{2L\ln(\alpha_E)} \\
&\cdot \Big(\frac{\partial^2 Q_1(x, T_2)}{\partial x^2}\int_0^L (\widehat{v}_{,x}^+)^2 \mathrm{d}x + 2\widehat{v}_{,xx}^+ \int_0^L \widehat{v}_{,x}^+ \frac{\partial Q_1(x, T_2)}{\partial x}\mathrm{d}x\Big) \\
&= R_1 A_1(T_2)^2 \overline{A}_1(T_2) + R_2 \mathrm{D}_2 A_1(T_2) + R_3 A_1(T_2) + R_4 \overline{A}_1(T_2) + R_5 \overline{A}_1(T_2)\mathrm{e}^{\mathrm{i}\sigma T_2}.
\end{aligned} \tag{30}
$$

Two secular term equations can be obtained by the inner product of Eq. (30), which are written in the matrix as follows:

$$\begin{pmatrix} S_1 & S_2 - \mathrm{i}S_3 \\ S_2 + \mathrm{i}S_3 & S_4 \end{pmatrix}\begin{pmatrix} q_{1,1}(T_2) \\ q_{1,2}(T_2) \end{pmatrix} = \begin{pmatrix} H_1 \\ H_2 \end{pmatrix}, \tag{31}$$

where S_i and H_i are given in Appendix A. Replace any column in the coefficient matrix with a column vector H, and take the determinant to be zero. Then, the solvability condition of the gyroscopic system is obtained by[48]

$$H_1 S_4 - H_2(S_2 - \mathrm{i}S_3) = 0. \tag{32}$$

The polar coordinate form of the introduced response A_1 is

$$A_1(T_2) = \frac{1}{2}a(T_2)\mathrm{e}^{\mathrm{i}\theta(T_2)}, \tag{33}$$

where $a(T_2)$ is the amplitude, and $\theta(T_2)$ is the phase angle.

Introduce

$$\beta(T_2) = T_2\sigma - 2\theta(T_2). \tag{34}$$

Then, with the steady-state response, we have

$$\mathrm{D}_2 a(T_2) = 0, \quad \mathrm{D}_2\beta(T_2) = 0. \tag{35}$$

Substituting Eqs. (33)–(35) into the solvability condition (32) yields the amplitude-frequency response equations with the phase angle as follows:

$$\begin{cases} a(\Xi_{11}(\sigma, \Gamma_1)\sin\beta + \Xi_{12}(\sigma, \Gamma_1)\cos\beta + \Xi_{13}(\sigma) + \Xi_{14}a^2) = 0, \\ a(\Xi_{21}(\sigma, \Gamma_1)\sin\beta + \Xi_{22}(\sigma, \Gamma_1)\cos\beta + \Xi_{23}(\sigma) + \Xi_{24}a^2) = 0. \end{cases} \tag{36}$$

Eliminate the phase angle β. Then, we have $\zeta_1 a^4 + \zeta_2 a^2 + \zeta_3 = 1$. Finally, the solution of each order scale is substituted back into Eq. (11), with which the total response of any position of the AFG pipe can be obtained.

3.2 DQEM

To verify the approximate analytical solution obtained by the direct multi-scale method, the DQEM is adopted. On the basis of the differential element method (DQM), the DQEM introduces rotation angles at both ends of the pipe as new generalized variables. Therefore, it has N nodes and $N + 2$ variables. With $N - 2$ interior point equations and 4 boundary conditions, the fourth-order boundary-value problem can be solved[49]. The detailed procedure is shown in Appendix B[50]. The DQEM needs to select nodes with a reasonable distribution. According to Ref. [51], a non-uniform distribution of nodes can improved the calculation accuracy and convergence. Therefore, this paper employs the Chebyshev-Gauss-Lobatto non-uniform distribution as follows:

$$x_i = \frac{1}{2}\Big(1 - \cos\frac{(i-1)\pi}{N-1}\Big)L, \quad i = 1, 2, \cdots, N. \tag{37}$$

References [52] and [53] show that for simple modes, the DQEM with only five nodes has good convergence. The simulation employs a total of 11 nodes ($N = 11$) to enhance the accuracy of the obtained results. The initial conditions for the DQEM are given as follows:

$$v_i = 0.000\,1\sin(2\pi x_i), \quad v_{i,t} = 0, \quad i = 2, 3, \cdots, N - 1. \tag{38}$$

4 Case studies

According to the method introduced, the parametric resonance analysis of the case is carried out, the stability boundary of the parametric resonance of the AFG pipe is solved by the direct multi-scale method, and the amplitude-frequency response results are verified by the DQEM. In addition, the influence of gradient on the parametric resonance is analyzed.

4.1 Parametric resonance in the subcritical region

In this section, the parametric resonance of the AFG pipe in the subcritical region is studied, and the influence of gradient on the vibration of the subcritical pipe is analyzed.

4.1.1 Amplitude-frequency response

Based on Eq. (3), the Jacobi matrix of amplitude a and phase angle β is extracted. The characteristic equation of the matrix is $\lambda^2 + c_1\lambda + c_2 = 0$. When the real parts of the eigenvalues are all negative, there will be no power exponent increasing infinitely with time. Therefore, according to the Routh-Hurwitz criterion, all the coefficients in the equation are positive, which means $c_1 > 0$ and $c_2 > 0$.

Figure 2 shows the stability boundary and response characteristics of the AFG pipe in the subcritical region. Figure 2(a) shows the critical pulsating flow velocity boundary for the
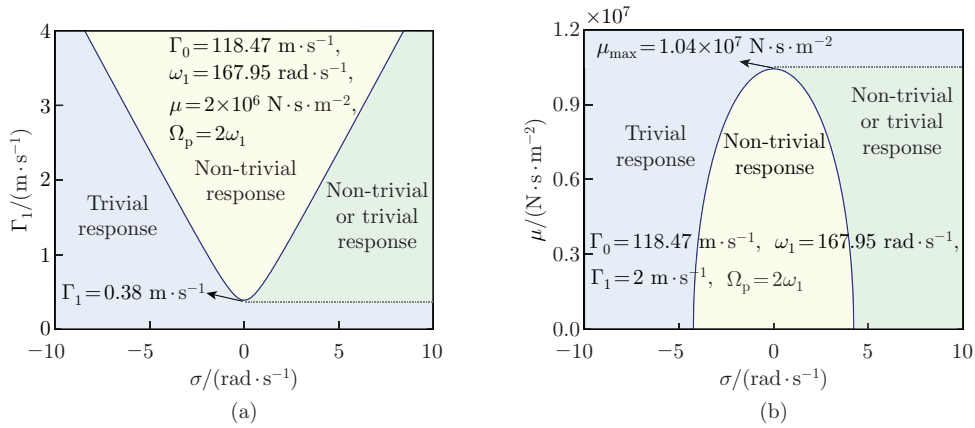

Fig. 2 Parametric resonance boundaries in the subcritical region: (a) pulsating flow velocity boundaries; (b) damping boundaries (color online)

parametric resonance. When the pulsating flow velocity exceeds $0.38\,\mathrm{m\cdot s^{-1}}$, the response bifurcates into non-trivial and trivial solutions. The frequency range corresponding to any pulsating flow velocity is the bandwidth of the unstable zero solution in the response. The frequency range corresponding to any pulsating flow velocity is the bandwidth of the unstable zero solution in the response. Figure 2(b) shows the influence of damping on the response. When the damping exceeds $1.04 \times 10^7\,\mathrm{N\cdot s\cdot m^{-2}}$, the parametric resonance response disappears.

Under the stability boundary, the steady-state response of the parametric vibration of the AFG pipe is analytically solved and numerically verified. Figure 3(a) shows the time history obtained by the DQEM. Figure 3(b) shows the numerical and analytical solutions. The average flow velocity is $118.47\,\mathrm{m\cdot s^{-1}}$ (the data are selected from $\Gamma_{0\text{-sub}}$ when $\alpha_E = 1.2$ in Table 1), and the pulsating flow velocity is $2\,\mathrm{m\cdot s^{-1}}$. Obviously, the approximate analytical solution is verified.
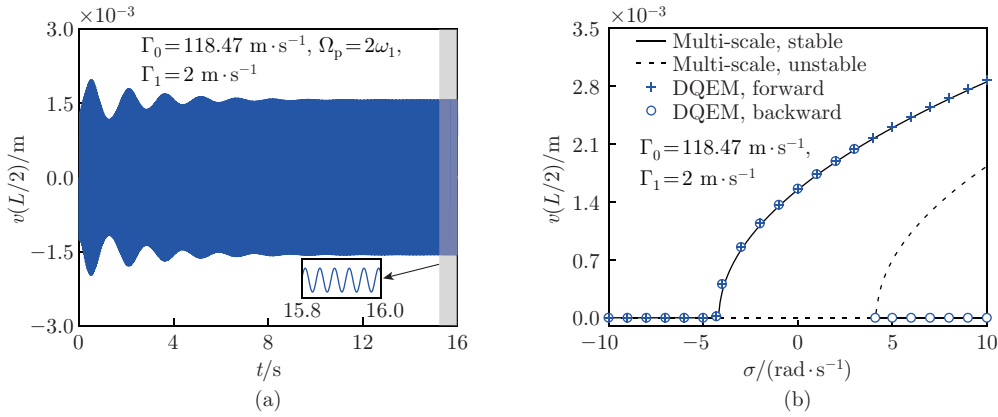
Fig. 3   Total responses of parametric resonance at the midpoint of the subcritical pipe: (a) time history via the DQEM; (b) numerical and analytical solutions (color online)

Figure 4 shows the total responses of the pipe at different pulsating flow velocities ($\Gamma_1 = 1\,\mathrm{m\cdot s^{-1}}$, $\Gamma_1 = 2\,\mathrm{m\cdot s^{-1}}$, and $\Gamma_1 = 3\,\mathrm{m\cdot s^{-1}}$). The average flow velocity at all the three gradient parameters is $118.47\,\mathrm{m\cdot s^{-1}}$. Figure 4(a) shows that for these three gradient parameters, the three selected pulsating flow velocities are within the range that can cause parametric vibration. When the gradient parameter is 1, it is a homogeneous pipe. Obviously, the existence of Young's modulus gradient affects the bandwidth of the unstable zero solution compared with the homogeneous pipe. Moreover, increasing the gradient parameter improves the condition of parametric vibration. As shown in Figs. 4(b), 4(c), and 4(d), the pulsating flow velocity will affect the parametric resonance amplitude and resonance region. At the same average flow velocity, the amplitude of the total response and the resonance region increase as the pulsating flow velocity increases.

4.1.2   Influence of gradient on parametric resonance

To further clarify the influence of Young's modulus gradient on the subcritical parametric resonance, the parametric response at $0.25L$ and $0.75L$ of the pipe is discussed in Fig. 5. The selected gradient parameters are 0.4, 0.8, 1.2, and 1.6. The average flow velocity is $118.47\,\mathrm{m\cdot s^{-1}}$, and the pulsating flow velocity is $2\,\mathrm{m\cdot s^{-1}}$. It can be seen that the existence of Young's modulus gradient and fluid make the symmetrical position of the pipe produce asymmetric responses. To describe the asymmetry more clearly, the relative deviation of the responses is defined for the non-trivial solution as follows:

$$R_\mathrm{e} = \left| \frac{v_{0.25L} - v_{0.75L}}{v_{0.75L}} \right|, \tag{39}$$
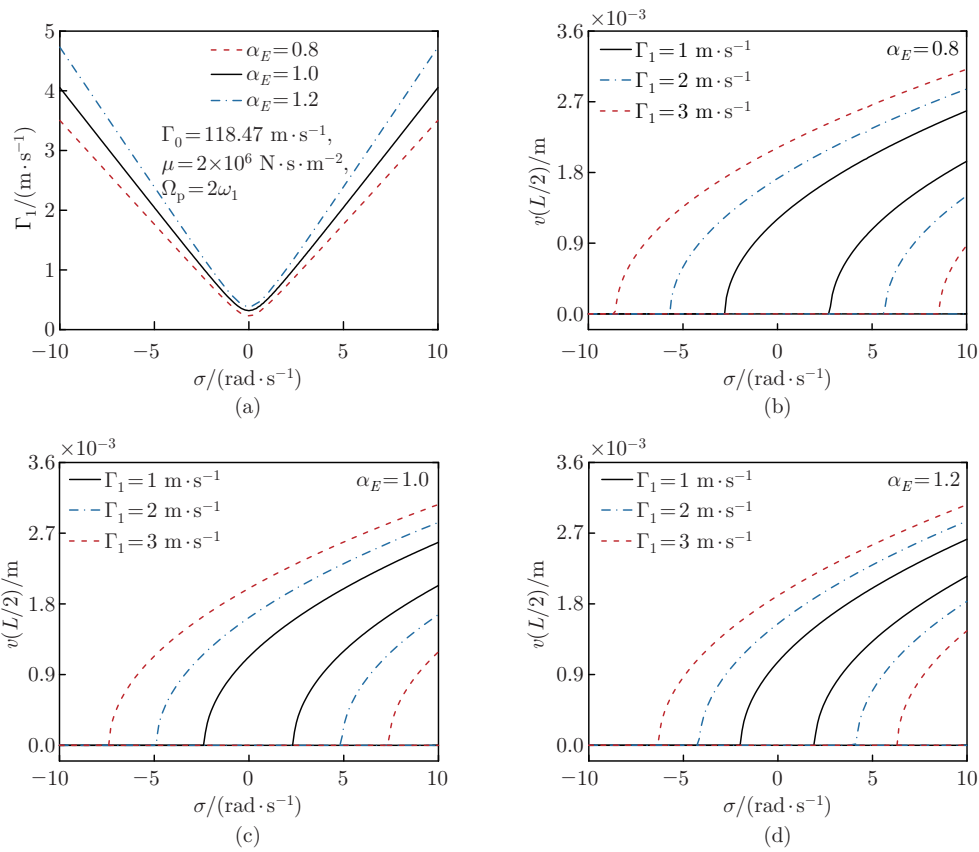
Fig. 4   (a) Pulsating flow velocity boundary under different α_E. Total responses of the pipe under different pulsating flow velocities at (b) $\alpha_E = 0.8$, (c) $\alpha_E = 1.0$, and (d) $\alpha_E = 1.2$ (color online)
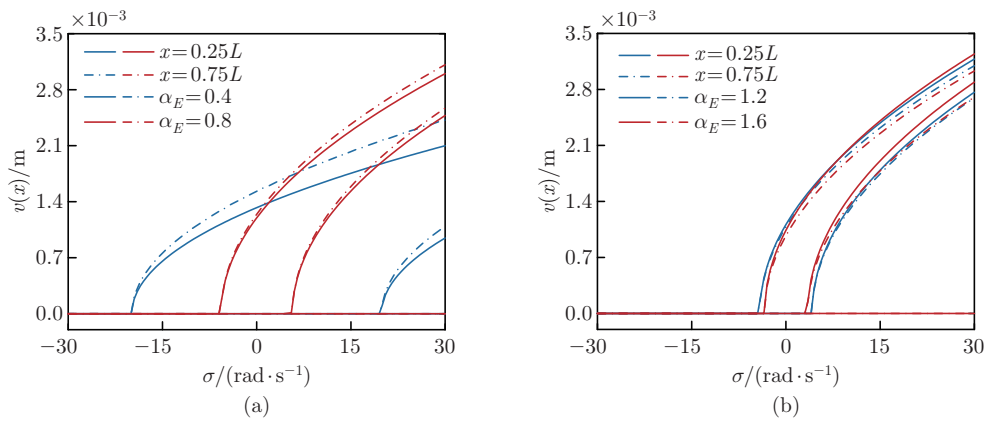

Fig. 5   Responses of the subcritical pipe at $0.25L$ and $0.75L$ under (a) $\alpha_E = 0.4$, 0.8 and (b) $\alpha_E = 1.2$, 1.6 (color online)

where $v_{0.25L}$ and $v_{0.75L}$ represent the amplitudes at $0.25L$ and $0.75L$, respectively. $R_{\text{e-s}}$ and $R_{\text{e-uns}}$ in Fig. 6 represent the relative deviations of the stable and unstable solutions, respectively. It can be seen that when the gradient parameter is less than 1, the decrease in α_E enhances the asymmetry. This is contrary when the gradient parameter is greater than 1.
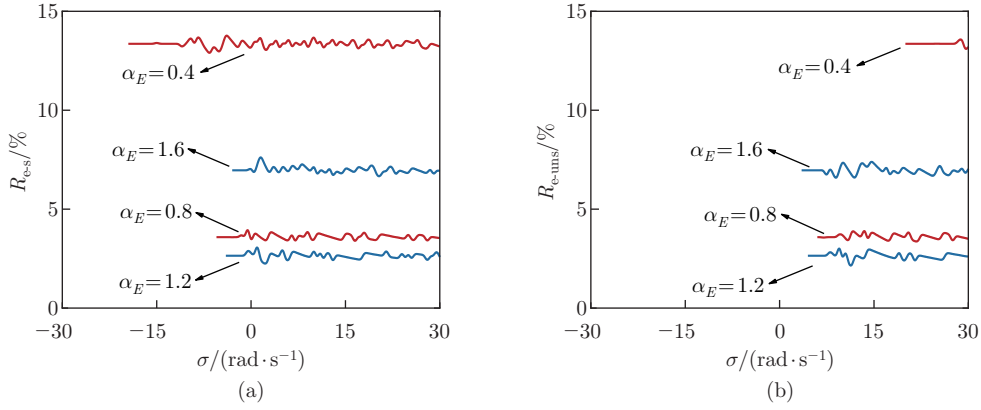
Fig. 6 Relative deviations of the non-trivial response at $0.25L$ and $0.75L$ of the subcritical pipe: (a) stable solution; (b) unstable solution (color online)

4.2 Parametric resonance in the supercritical region

In this section, the parametric resonance of the AFG pipe in the supercritical region is studied, the influence of gradient is analyzed, and the resonance responses of the pipe in the subcritical and supercritical regions are compared.

4.2.1 Amplitude-frequency response

Figure 7 shows the stability boundary and response characteristics of the pipe in the supercritical region. Figure 7(a) shows that when the pulsating velocity exceeds $0.22\,\mathrm{m\cdot s^{-1}}$, the responses will bifurcate into trivial and non-trivial solutions. As shown in Fig. 7(b), the parametric responses disappear when the damping exceeds $1.82 \times 10^7\,\mathrm{N \cdot s/m^2}$. From Figs. 2 and 7, it can be observed that greater damping is required to suppress the parametric responses in the supercritical AFG pipes. Therefore, the parametric responses caused by the velocity pulsation are more intense and harder to be suppressed in the supercritical region.
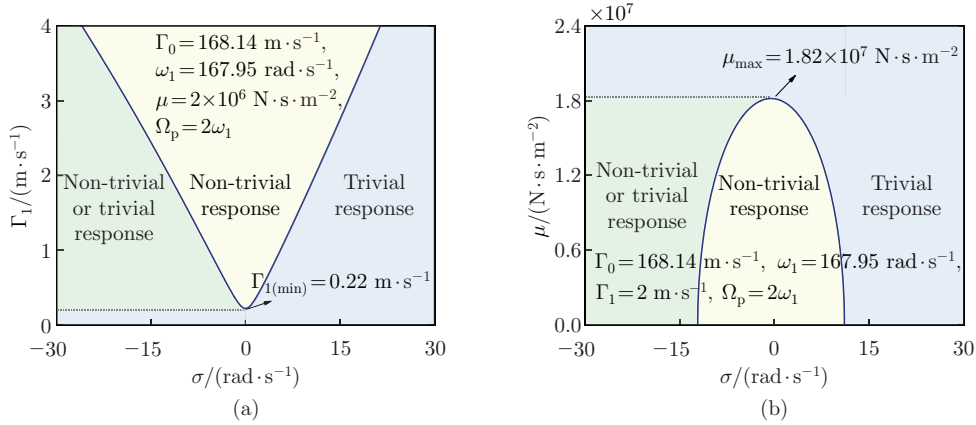

Fig. 7 Parametric resonance boundaries in the supercritical region: (a) pulsating flow velocity boundaries; (b) damping boundaries (color online)

Figure 8 shows the time history responses of the parametric vibration in the supercritical region obtained by the DQEM. The average flow velocity is $168.14\,\mathrm{m\cdot s^{-1}}$ (the data are selected from $\Gamma_{0\text{-sup}}$ when $\alpha_E = 1.2$ in Table 1), and the pulsating flow velocity is $2\,\mathrm{m\cdot s^{-1}}$. Similarly, the initial conditions of the DQEM are the same as those in Eq. (39). Different from the subcritical region, the introduction of non-trivial equilibrium configuration makes the supercritical pipe have zero shift.
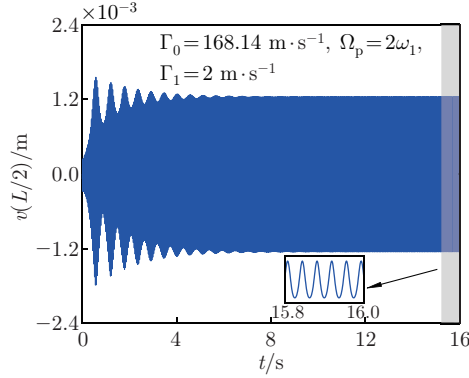
Fig. 8 Time history of the supercritical pipe via the DQEM (color online)

In addition, the buckled configuration brings square nonlinearity, which makes the super-critical AFG pipe have responses on the T_1 scale. To study the responses of the supercritical AFG pipe more comprehensively, Figs. 9(a)–9(d) show the components of the solutions at different scales. According to Eq. (11), the total response in Fig. 9(e) is obtained by summing the responses at the T_0 and T_1 scales. To further analyze the broadband response, the broadband response at the midpoint of the pipe is verified numerically. The results are shown in Fig. 9(e). Therefore, the analytical solution is verified by the DQEM. In addition, the non-primary resonance response in the supercritical region is not equal to zero. Although the zero-shift component is negative, the solution at the T_0 scale, the natural frequency component at the T_1 scale, and the external excitation frequency component are all positive. Therefore, the positive non-primary resonance responses are obtained by superposition.
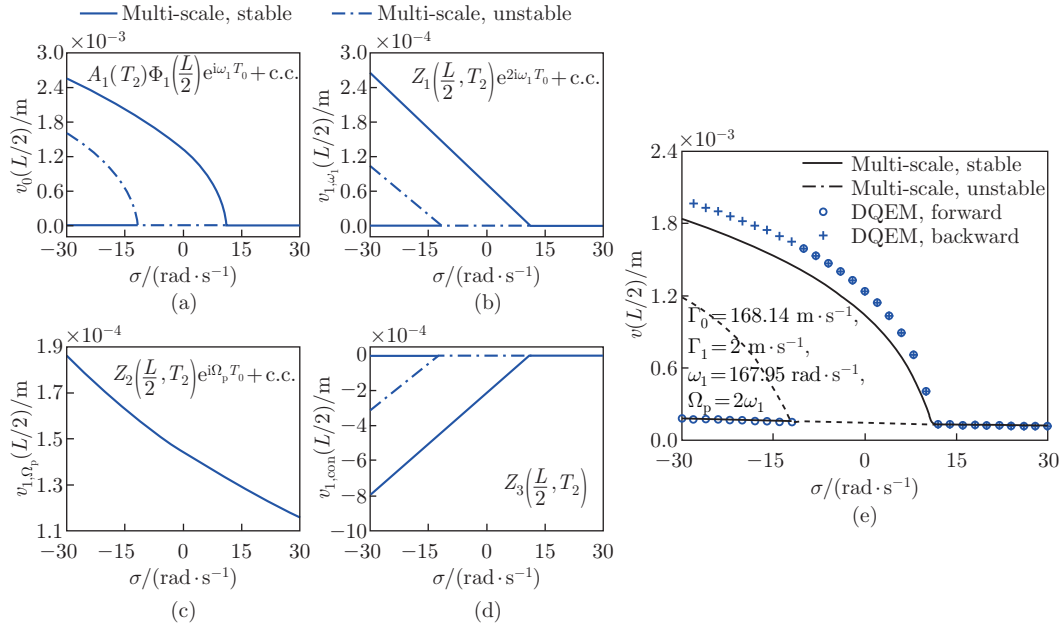

Fig. 9 Analyses of (a) the solution of the midpoint at the T_0 scale, (b) the natural frequency component of the midpoint at the T_1 scale, (c) the external excitation frequency component of the midpoint at the T_1 scale, (d) the zero-shift component of the midpoint at the T_1 scale, and (e) the synthesis of the T_0 and T_1 scale solutions (color online)

Figure 10 shows the total responses at the midpoint of the supercritical pipe. The selected pulsating flow velocities are $1\,\mathrm{m\cdot s^{-1}}$, $2\,\mathrm{m\cdot s^{-1}}$, and $3\,\mathrm{m\cdot s^{-1}}$. The average flow velocity at all the three gradient parameters is $168.14\,\mathrm{m\cdot s^{-1}}$. The existence of Young's modulus gradient affects the bandwidth of the unstable solution. At the same average flow velocity, the amplitude of the total response and the resonance region increase as the pulsating flow velocity increases.
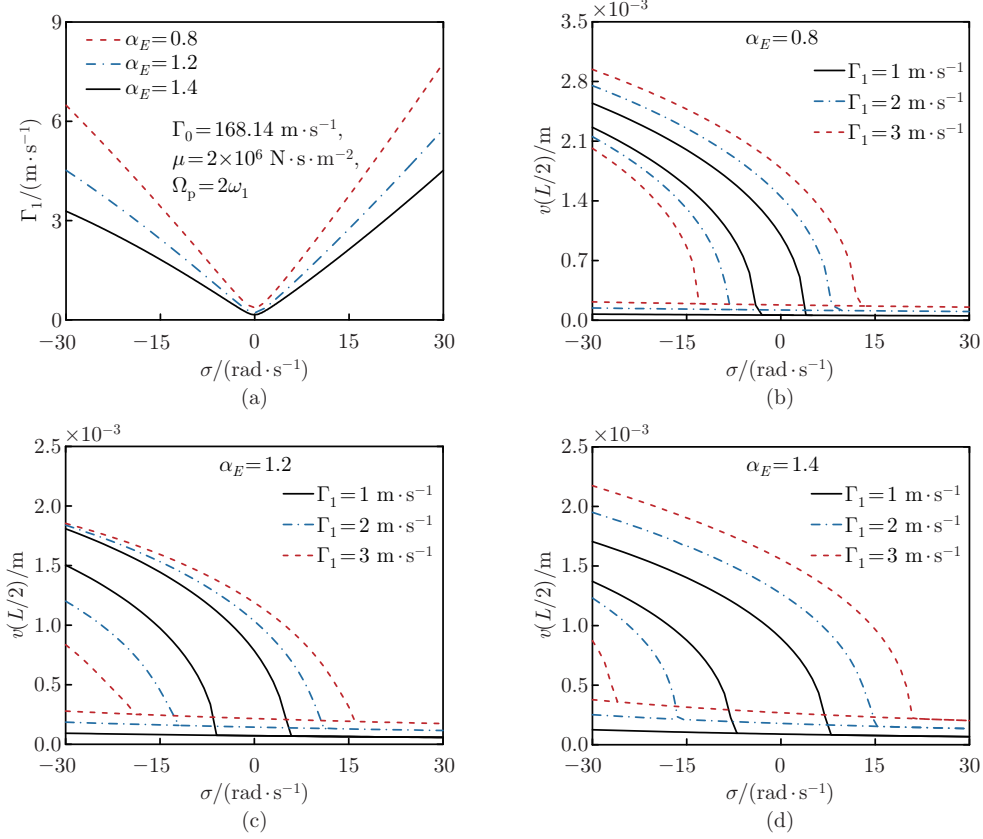
Fig. 10 (a) Pulsating flow velocity boundaries at different α_E. Total responses at (b) $\alpha_E = 0.8$, (c) $\alpha_E = 1.2$, and (d) $\alpha_E = 1.4$ (color online)

4.2.2 Influence of gradient on the parametric resonance

Figure 11 shows the influence of Young's modulus gradient on the supercritical parametric resonance. The gradient parameters are 0.4, 0.8, 1.2, and 1.6. To further explore the influence of the gradient parameter on the symmetric positional response of the supercritical pipe, the relative deviation of the response is defined according to Eq. (42). As shown in Fig. 12, the decrease in α_E can enhance the asymmetry of the response when α_E is less than 1. This is contrary when α_E is greater than 1.

4.2.3 Comparison of parametric resonance in the subcritical and supercritical regions

To compare the influence of Young's modulus gradient on the parametric resonance of the pipe in the subcritical and supercritical regions, the parameter values are selected as shown in Table 2. It is worth noting that the supercritical average flow velocity selected for each gradient parameter is determined according to $\Gamma_{0\text{-sup}} = 1.1\Gamma_{0\text{-cr}}$.

The stability boundaries of the pipe in the subcritical and supercritical regions with different gradient parameters are shown in Figs. 13 and 14. Meanwhile, the relationship between the gradient parameter and the critical pulsating flow velocity in the subcritical and supercritical regions is clearly shown in Fig. 13(b). The maximum and minimum gradient parameters in
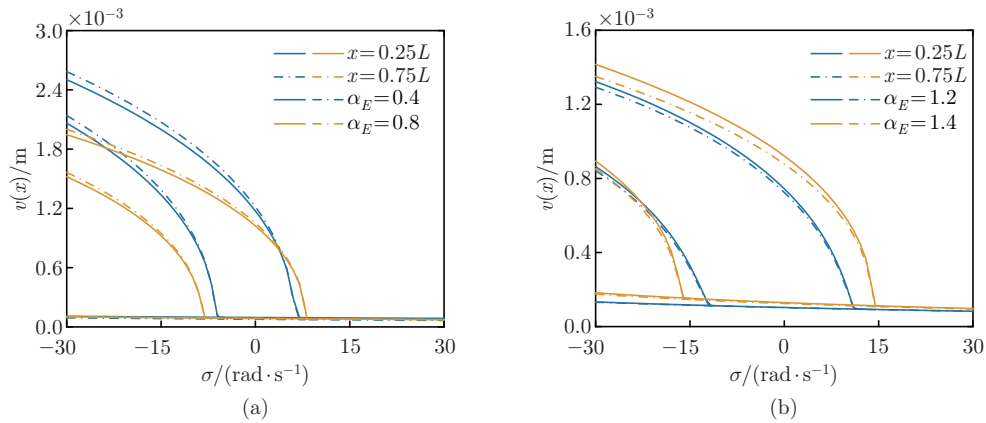
Fig. 11   Responses of the supercritical pipe at $0.25L$ and $0.75L$ under (a) $\alpha_E = 0.4$, 0.8 and (b) $\alpha_E = 1.2$, 1.4 (color online)
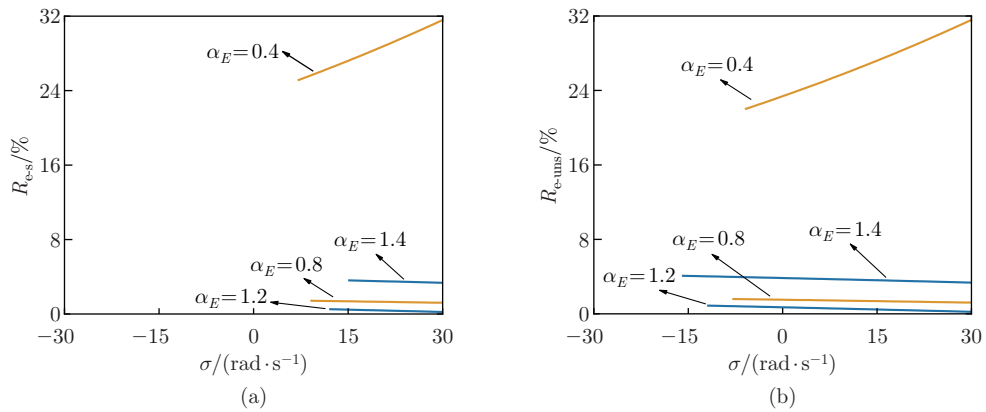

Fig. 12   Relative deviations of the parametric response at $0.25L$ and $0.75L$ of the supercritical pipe: (a) stable solution; (b) unstable solution (color online)

Table 2   Comparison of parametric vibration in the subcritical and supercritical regions ($\Gamma_{0\text{-sup}} = 1.1\Gamma_{0\text{-cr}}$)

α_E	$\Gamma_1/(\text{m·s}^{-1})$	$\mu/(\text{N·s·m}^{-2})$	$\omega_1/(\text{rad·s}^{-1})$	$\Gamma_{0\text{-sub}}/(\text{m·s}^{-1})$	$\Gamma_{0\text{-sup}}/(\text{m·s}^{-1})$
0.4	2	2×10^6	131.00	93.69	132.13
0.8	2	2×10^6	151.79	107.20	152.10
1.2	2	2×10^6	167.95	118.47	168.14
1.4	2	2×10^6	175.20	123.50	175.29

Fig. 13(b) are selected for a detailed analysis, which are shown in Figs. 13(a) and 13(c). Figure 14 does the same work. The comparison shows that the pipe is more sensitive to external excitation in the supercritical region. Under the same condition, a smaller critical pulsating flow velocity in the supercritical region can cause parametric resonance, and increasing the damping coefficient can effectively suppress the parametric resonance. Meanwhile, the bandwidth of the unstable solution of the supercritical pipe will be narrower. In addition, the increase in Young's modulus gradient can improve the critical pulsating flow velocity causing parametric resonance and reduce the sensitivity of the pipe to external excitation. However, at the same natural frequency, the supercritical pipe remains more sensitive to the pulsating excitation.
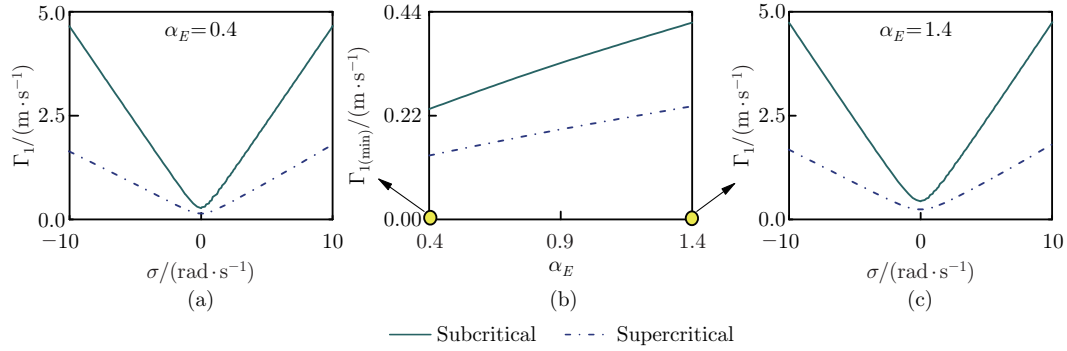
Fig. 13 Pulsating flow velocity boundaries of the pipe at (a) $\alpha_E = 0.4$ and (c) $\alpha_E = 1.4$. (b) Relationship between the gradient parameter and the pulsating flow velocity boundaries (color online)
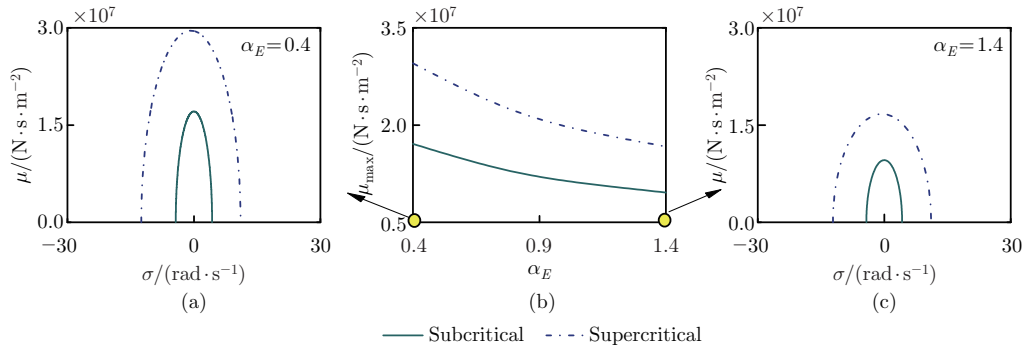

Fig. 14 Damping boundaries of the pipe at (a) $\alpha_E = 0.4$ and (c) $\alpha_E = 1.4$. (b) Relationship between the gradient parameter and the damping boundaries (color online)

Figure 15 compares the parametric resonance of the pipe in the subcritical and supercritical regions. The selected gradient parameters are 0.4, 0.8, 1.2, and 1.4. The solid lines and dashed lines in the figure correspond to stable branches and unstable branches, respectively. It can be seen that the cubic nonlinearity plays a dominant role in the subcritical region. It shows the hard characteristic of bending to the right. In the supercritical region, the introduction of the buckled configuration produces square nonlinearity. Therefore, it shows a soft characteristic of bending to the left. On the contrary to the subcritical region, the increase in α_E reduces the response amplitude of the pipe in the supercritical region, but the resonance region increases.

5 Conclusions

In this paper, the nonlinear governing equation for the parametric vibration of a simply supported AFG pipe is established. The stability boundaries and amplitude-frequency responses are obtained by the direct multi-scale method. The approximate analytical results are verified by the DQEM. The influence of Young's modulus gradient on the parametric resonance is investigated. Some conclusions are obtained as follows.

(i) The non-trivial equilibrium configuration makes the AFG pipe change from hard to soft, and more frequency components are introduced into the solution. Different from the subcritical pipe, the non-primary resonance response of the supercritical pipe is not zero.

(ii) The velocity pulsation-induced parametric response is more intense and harder to be suppressed in the supercritical region. Based on the same fundamental frequency, to suppress
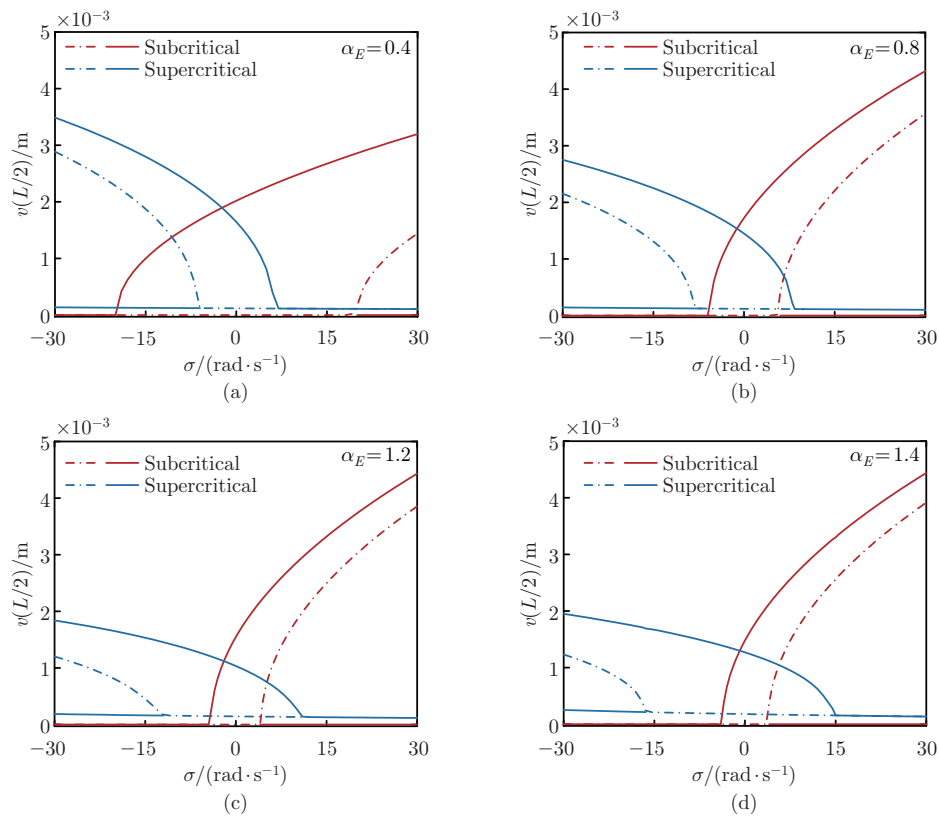
Fig. 15   Parametric responses at (a) $\alpha_E = 0.4$, (b) $\alpha_E = 0.8$, (c) $\alpha_E = 1.2$, and (d) $\alpha_E = 1.4$ before and after buckling (color online)

the parametric response, the supercritical AFG pipe needs greater damping. In addition, the increase in Young's modulus gradient can reduce the sensitivity of the pipe to the parametric excitation and improve the stability of the pipe.

(iii) The existence of Young's modulus gradient and fluid make the symmetrical position of the pipe produce asymmetric responses. When the temperature increases along the axial direction, reducing α_E can enhance the asymmetry of the parametric responses.

Conflict of interest   Hu DING and Liqun CHEN are editorial board members for *Applied Mathematics and Mechanics* (*English Edition*) and were not involved in the editorial review or the decision to publish this article. The authors declare no conflict of interest.

Open access   This article is licensed under a Creative Commons Attribution 4.0 International License, which permits use, sharing, adaptation, distribution and reproduction in any medium or format, as long as you give appropriate credit to the original author(s) and the source, provide a link to the Creative Commons licence, and indicate if changes were made. To view a copy of this licence, visit http://creativecommons.org/licenses/by/4.0/.

Author contributions   All authors contributed to the study conception and design. Material preparation, data collection and analysis were performed by Jie JING and Xiaoye MAO. The first draft of the manuscript was written by Jie JING and all authors commented on previous versions of the manuscript. All authors read and approved the final manuscript.

Data availability   The datasets generated and/or analyzed during the current study are available from the corresponding author on reasonable request.

References

[1] IBRAHIM, R. A. Overview of mechanics of pipes conveying fluids — part I: fundamental studies. *Journal of Pressure Vessel Technology*, **132**, 034001 (2010)

[2] ALI, H. H., MUSTAFA, A. W., and AL-BAKRI, F. F. A new control design and robustness analysis of a variable speed hydrostatic transmission used to control the velocity of a hydraulic cylinder. *International Journal of Dynamics and Control*, **9**(3), 1078–1091 (2020)

[3] GAO, P. X., YU, T., ZHANG, Y. L., WANG, J., and ZHAI, J. Y. Vibration analysis and control technologies of hydraulic pipeline system in aircraft: a review. *Chinese Journal of Aeronautics*, **34**(4), 83–114 (2021)

[4] GUO, X. M., CAO, Y. M., MA, H., XIAO, C. L., and WEN, B. C. Dynamic analysis of an L-shaped liquid-filled pipe with interval uncertainty. *International Journal of Mechanical Sciences*, **217**, 107040 (2022)

[5] LI, M., XU, Q., CHEN, X. C., ZHANG, X. L., and LI, Y. H. Modeling and modal analysis of non-uniform multi-span oil-conveying pipes with elastic foundations and attachments. *Applied Mathematical Modelling*, **88**, 661–675 (2020)

[6] LIANG, F., GAO, A., LI, X. F., and ZHU, W. D. Nonlinear parametric vibration of spinning pipes conveying fluid with varying spinning speed and flow velocity. *Applied Mathematical Modelling*, **95**, 320–338 (2021)

[7] PAÏDOUSSIS, M. P. and ISSID, N. T. Dynamic stability of pipes conveying fluid. *Journal of Sound and Vibration*, **33**(3), 267–294 (1974)

[8] PLAUT, R. H. and HUSEYIN, K. Instability of fluid conveying pipes under axial load. *Journal of Applied Mechanics*, **42**(4), 889–890 (1975)

[9] MATSUZAKI, Y. and FUNG, Y. C. Nonlinear stability analysis of a two-dimensional model of an elastic tube conveying a compressible flow. *Journal of Applied Mechanics*, **46**(1), 31–36 (1979)

[10] PANDA, L. N. and KAR, R. C. Nonlinear dynamics of a pipe conveying pulsating fluid with combination, principal parametric and internal resonances. *Journal of Sound and Vibration*, **309**(3-5), 375–406 (2008)

[11] BURAK-ÖZHAN, B. and PAKDEMIRLI, M. Principal parametric resonances of a general continuous system with cubic nonlinearities. *Applied Mathematics and Computation*, **219**(5), 2412–2423 (2012)

[12] ZHU, B., GUO, Y., ZHAO, T., and LI, X. Nonlinear dynamics of inclined viscoelastic pipes subjected to pulsatile flow and multi-harmonic excitations. *Nonlinear Dynamics*, **111**(13), 11823–11849 (2023)

[13] SHAIK, N. H., SHARMA, A. K., and BHATTACHARYA, B. Effect of shape memory alloy actuation on parametric instability in pipes conveying pulsating fluid. *Journal of Vibration Engineering & Technologies*, **11**, 3003–3016 (2023)

[14] WEI, S., YAN, X., LI, X., DING, H., and CHEN, L. Q. Parametric vibration of a nonlinearly supported pipe conveying pulsating fluid. *Nonlinear Dynamics*, **111**(18), 16643–16661 (2023)

[15] GUO, X. M., GAO, P. X., MA, H., LI, H., WANG, B., HAN, Q. K., and WEN, B. C. Vibration characteristics analysis of fluid-conveying pipes concurrently subjected to base excitation and pulsation excitation. *Mechanical Systems and Signal Processing*, **189**, 110086 (2023)

[16] WANG, Y. K., TANG, M., YANG, M., and QIN, T. Three-dimensional dynamics of a cantilevered pipe conveying pulsating fluid. *Applied Mathematical Modelling*, **114**, 502–524 (2023)

[17] GUO, Y., ZHU, B., and LI, Y. H. Nonlinear dynamics of fluid-conveying composite pipes subjected to time-varying axial tension in sub- and super-critical regimes. *Applied Mathematical Modelling*, **101**, 632–653 (2022)

[18] ZHU, B., ZHANG, X., and ZHAO, T. Nonlinear planar and non-planar vibrations of viscoelastic fluid-conveying pipes with external and internal resonances. *Journal of Sound and Vibration*, **548**, 117558 (2023)

[19] XIE, W. D., LIANG, Z. L., JIANG, Z. Y., and ZHU, L. X. Dynamic responses of a flexible pipe conveying variable-density fluid and experiencing cross-flow and in-line coupled vortex-induced vibrations. *Ocean Engineering*, **260**, 111811 (2022)

[20] GHADIRIAN, H., MOHEBPOUR, S., MALEKZADEH, P., and DANESHMAND, F. Nonlinear free vibrations and stability analysis of FG-CNTRC pipes conveying fluid based on Timoshenko model. *Composite Structures*, **292**, 115637 (2022)

[21] XU, W. H., JIA, K., MA, Y. X., WANG, Y. Y., and SONG, Z. Y. Multispan classification methods and interaction mechanism of submarine pipelines undergoing vortex-induced vibration. *Applied Ocean Research*, **120**, 103027 (2022)

[22] LI, M. W., YAN, H., and WANG, L. Nonlinear model reduction for a cantilevered pipe conveying fluid: a system with asymmetric damping and stiffness matrices. *Mechanical Systems and Signal Processing*, **188**, 109993 (2023)

[23] DING, H., JI, J. C., and CHEN, L. Q. Nonlinear vibration isolation for fluid-conveying pipes using quasi-zero stiffness characteristics. *Mechanical Systems and Signal Processing*, **121**, 675–688 (2019)

[24] WEI, S., YAN, X., FAN, X., MAO, X. Y., DING, H., and CHEN, L. Q. Vibration of fluid-conveying pipe with nonlinear supports at both ends. *Applied Mathematics and Mechanics* (*English Edition*), **43**(6), 845–862 (2022) https://doi.org/10.1007/s10483-022-2857-6

[25] ZHOU, K., YI, H. R., DAI, H. L., YAN, H., GUO, Z. L., XIONG, F. R., NI, Q., HAGEDORN, P., and WANG, L. Nonlinear analysis of L-shaped pipe conveying fluid with the aid of absolute nodal coordinate formulation. *Nonlinear Dynamics*, **107**(1), 391–412 (2021)

[26] CHEN, F. J., CHEN, J. Y., DUAN, R. Q., HABIBI, M., and KHADIMALLAH, M. A. Investigation on dynamic stability and aeroelastic characteristics of composite curved pipes with any yawed angle. *Composite Structures*, **284**, 115195 (2022)

[27] MAKNUN, I. J., NATARAJAN, S., and KATILI, I. Application of discrete shear quadrilateral element for static bending, free vibration and buckling analysis of functionally graded material plate. *Composite Structures*, **284**, 115130 (2022)

[28] CHANDRASEKARAN, S., HARI, S., and AMIRTHALINGAM, M. Functionally graded materials for marine risers by additive manufacturing for high-temperature applications: experimental investigations. *Structures*, **35**, 931–938 (2022)

[29] ZHEN, Y. X., GONG, Y. F., and TANG, Y. Nonlinear vibration analysis of a supercritical fluid-conveying pipe made of functionally graded material with initial curvature. *Composite Structures*, **268**, 113980 (2021)

[30] ZHU, B., GUO, Y., CHEN, B., and LI, Y. H. Nonlinear nonplanar dynamics of porous functionally graded pipes conveying fluid. *Communications in Nonlinear Science and Numerical Simulation*, **117**, 106907 (2023)

[31] SELMI, A. and HASSIS, H. Vibration analysis of post-buckled fluid-conveying functionally graded pipe. *Composites Part C*: *Open Access*, **4**, 100117 (2021)

[32] JIN, Q., REN, Y., and YUAN, F. G. Combined resonance of pulsatile flow-transporting FG nanotubes under forced excitation with movable boundary. *Nonlinear Dynamics*, **111**(7), 6157–6178 (2022)

[33] DING, H. X., SHE, G. L., and ZHANG, Y. W. Nonlinear buckling and resonances of functionally graded fluid-conveying pipes with initial geometric imperfection. *The European Physical Journal Plus*, **137**(12), 1329 (2022)

[34] GUO, X. M., XIAO, C. L., GE, H., MA, H., LI, H., SUN, W., and LIU, Z. H. Dynamic modeling and experimental study of a complex fluid-conveying pipeline system with series and parallel structures. *Applied Mathematical Modelling*, **109**, 186–208 (2022)

[35] ZHAO, Y., FENG, J. M., ZHAO, B., ZHOU, S. M., TANG, Z., and PENG, X. Y. Vibration analysis and control of a screw compressor outlet piping system. *Proceedings of the Institution of Mechanical Engineers*, *Part E*: *Journal of Process Mechanical Engineering*, **233**(2), 403–411 (2018)

[36] DAI, J. Y., LIU, Y. S., LIU, H. C., MIAO, C. X., and TONG, G. J. A parametric study on thermo-mechanical vibration of axially functionally graded material pipe conveying fluid. *International Journal of Mechanics and Materials in Design*, **15**(4), 715–726 (2019)

[37] AN, C. and SU, J. Dynamic behavior of axially functionally graded pipes conveying fluid. *Mathematical Problems in Engineering*, **2017**, 6789634 (2017)

[38] LU, Z. Q., ZHANG, K. K., DING, H., and CHEN, L. Q. Nonlinear vibration effects on the fatigue life of fluid-conveying pipes composed of axially functionally graded materials. *Nonlinear Dynamics*, **100**(2), 1091–1104 (2020)

[39] GUO, Q., LIU, Y. S., CHEN, B. Q., and ZHAO, Y. Z. An efficient stochastic natural frequency analysis method for axially varying functionally graded material pipe conveying fluid. *European Journal of Mechanics-A/Solids*, **86**, 104155 (2021)

[40] TUO, Y. H., FU, G. M., SUN, B. J., LOU, M., and SU, J. Stability of axially functionally graded pipe conveying fluid: generalized integral transform solution. *Applied Ocean Research*, **125**, 103218 (2022)

[41] FAN, X., WU, N., LIU, Y., and GUO, Q. Resonance system reliability and sensitivity analysis method for axially FGM pipes conveying fluid with adaptive Kriging model. *Acta Mechanica Solida Sinica*, **35**(6), 1021–1029 (2022)

[42] AGHAZADEH, R. Stability analysis of fluid conveying axially functionally graded micro-pipes using a refined tube model. *Arabian Journal for Science and Engineering*, **47**(7), 8739–8750 (2022)

[43] AGHAZADEH, R. The effects of gravity and material gradation on the stability of axially functionally graded cantilevered pipes conveying fluid. *Journal of the Chinese Society of Mechanical Engineers*, **43**, 153–164 (2022)

[44] FU, G., TUO, Y., ZHANG, H., SU, J., SUN, B., WANG, K., and LOU, M. Effects of material characteristics on nonlinear dynamics of viscoelastic axially functionally graded material pipe conveying pulsating fluid. *Journal of Marine Science and Application*, **22**(2), 247–259 (2023)

[45] BABILIO, E. Dynamics of functionally graded beams on viscoelastic foundation. *International Journal of Structural Stability and Dynamics*, **14**(8), 1440014 (2014)

[46] MAO, X. Y., JING, J., DING, H., and CHEN, L. Q. Dynamics of axially functionally graded pipes conveying fluid. *Nonlinear Dynamics*, **111**(12), 11023–11044 (2023)

[47] FAN, X., ZHU, C. A., MAO, X. Y., and DING, H. Resonance regulation on a hydraulic pipe via boundary excitations. *International Journal of Mechanical Sciences*, **252**, 108375 (2023)

[48] CHEN, L. Q. and ZU, J. W. Solvability condition in multi-scale analysis of gyroscopic continua. *Journal of Sound and Vibration*, **309**(1-2), 338–342 (2008)

[49] WANG, X. W. and GU, H. Z. Static analysis of frame structures by the differential quadrature element method. *International Journal for Numerical Methods in Engineering*, **40**(4), 759–772 (1997)

[50] SHU, C., CHEW, Y. T., and RICHARDS, B. E. Generalized differential and integral quadrature and their application to solve boundary layer equations. *International Journal for Numerical Methods in Fluids*, **21**(9), 723–733 (1995)

[51] DING, H., YAN, Q. Y., and ZU, J. W. Chaotic dynamics of an axially accelerating viscoelastic beam in the supercritical regime. *International Journal of Bifurcation and Chaos*, **24**(5), 1450062 (2014)

[52] WANG, X. W. and WANG, Y. L. Free vibration analysis of multiple-stepped beams by the differential quadrature element method. *Applied Mathematics and Computation*, **219**(11), 5802–5810 (2013)

[53] WANG, Y. L., WANG, X. W., and ZHOU, Y. Static and free vibration analyses of rectangular plates by the new version of the differential quadrature element method. *International Journal for Numerical Methods in Engineering*, **59**(9), 1207–1226 (2004)

Appendix A

The coefficients $p_{n,k}$ in Eq. (21) are

$$
\begin{cases}
p_{1,1} = 1, \quad p_{1,2} = \dfrac{1\,000(3.476\,203\,39 \times 10^8 \omega_1^2 - 1.077\,743\,775 \times 10^{13})}{7.751\,069\,827 \times 10^9 \omega_1^2 - 2.874\,374\,389 \times 10^{15} - 9.948\,972\,650 \times 10^{13}\mathrm{i}\omega_1}, \\[3mm]
\bar{p}_{1,1} = 1, \quad \bar{p}_{1,2} = \dfrac{1\,000(3.476\,203\,39 \times 10^8 \omega_1^2 - 1.077\,743\,775 \times 10^{13})}{7.751\,069\,827 \times 10^9 \omega_1^2 - 2.874\,374\,389 \times 10^{15} + 9.948\,972\,650 \times 10^{13}\mathrm{i}\omega_1}.
\end{cases}
\tag{A1}
$$

The specific forms of S_i and H_i in Eq. (31) are

$$S_1 = \frac{\pi^4 E_0 I_p (\alpha_E + 1) - 2\pi^2 L^2 (\rho_f A_f \Gamma_0^2 - P_0) - \omega_1^2 L^4 (\rho_0 A_p (\alpha_\rho + 1) + 2\rho_f A_f)}{4L^3}$$
$$+ \frac{\pi^4 E_0 A_p (\alpha_E - 1)(4B_2^2 + 3B_1^2)}{8L^3 \ln(\alpha_E)}, \tag{A2}$$

$$S_2 = \frac{\pi^4 E_0 A_p B_1 B_2 (\alpha_E - 1)}{L^3 \ln(\alpha_E)} - \frac{32\pi^2 E_0 I_p (\alpha_E - 1)}{9L^3} + \frac{8\omega_1^2 \rho_0 A_p L (\alpha_\rho - 1)}{9\pi^2}, \tag{A3}$$

$$S_3 = \frac{8\omega_1 \rho_f A_f \Gamma_0}{3}, \tag{A4}$$

$$S_4 = \frac{16\pi^4 E_0 I_p (\alpha_E + 1) - 8\pi^2 L^2 (\rho_f A_f \Gamma_0^2 - P_0) - \omega_1^2 L^4 (\rho_0 A_p (\alpha_\rho + 1) + 2\rho_f A_f)}{4L^3}$$
$$+ \frac{\pi^4 E_0 A_p (\alpha_E - 1)(24B_2^2 + 2B_1^2)}{4L^3 \ln(\alpha_E)}, \tag{A5}$$

$$H_1 = -\big(3\pi^4 E_0 A_p (\alpha_E - 1)((3B_1 \overline{p}_{1,1} + 4B_2 \overline{p}_{1,2})s_{2,1}(T_2) + 4(B_1 \overline{p}_{1,2} + B_2 \overline{p}_{1,1})s_{2,2}(T_2))$$
$$+ 2L^2 \ln(\alpha_E)\rho_f A_f \Gamma_1 (3\mathrm{i}\pi^2 \Gamma_0 \overline{p}_{1,1} - 4L\varepsilon^2 \sigma \overline{p}_{1,2})\big)\big/(12L^3 \ln(\alpha_E))\overline{A}_1(T_2)\mathrm{e}^{\mathrm{i}\sigma T_2}$$
$$+ \frac{48\pi^2 \rho_f A_f \Gamma_0 p_{1,2} - \mathrm{i}\omega_1 L(9\pi^2 p_{1,1}(\rho_0 A_p (\alpha_\rho + 1) + 2\rho_f A_f) - 32\rho_0 A_p p_{1,2}(\alpha_\rho - 1))}{18\pi^2}$$
$$\cdot \mathrm{D}_2 A_1(T_2) - \frac{\pi^4 E_0 A_p (\alpha_E - 1)}{8L^3 \ln(\alpha_E)}((3p_{1,1}^2 + 4p_{1,2}^2)\overline{p}_{1,1} + 8p_{1,2}\overline{p}_{1,2}p_{1,1})\overline{A}_1(T_2)A_1(T_2)^2$$
$$+ \big(\mathrm{i}\omega_1 \mu\pi^2 \langle 256 I_p p_{1,2}(\alpha_E - 1)\ln(\alpha_E) - 9\pi^2 (2I_p p_{1,1}(\alpha_E + 1)\ln(\alpha_E)$$
$$+ A_p(\alpha_E - 1)((3B_1^2 + 4B_2^2)p_{1,1} + 8B_1 B_2 p_{1,2}))\rangle\big)\big/(72L^3 \ln(\alpha_E))A_1(T_2)$$
$$- \frac{\pi^4 E_0 A_p (\alpha_E - 1)((3B_1 p_{1,1} + 4B_2 p_{1,2})s_{3,1}(T_2) + 4(B_1 p_{1,2} + B_2 p_{1,1})s_{3,2}(T_2))}{4L^3 \ln(\alpha_E)}A_1(T_2)$$
$$- \big(\pi^4 E_0 A_p (\alpha_E - 1)((3s_{1,1}(T_2)B_1 \overline{p}_{1,1} + 4s_{1,1}(T_2)B_2 \overline{p}_{1,2})$$
$$+ 4(s_{1,2}(T_2)B_1 \overline{p}_{1,2} + s_{1,2}(T_2)B_2 \overline{p}_{1,1}))\big)\big/(4L^3 \ln(\alpha_E))\overline{A}_1(T_2), \tag{A6}$$

$$H_2 = -\big(3\pi^4 E_0 A_p (\alpha_E - 1)((B_1 \overline{p}_{1,2} + B_2 \overline{p}_{1,1})s_{2,1}(T_2) + (B_1 \overline{p}_{1,1} + 12B_2 \overline{p}_{1,2})s_{2,2}(T_2))$$
$$+ (6\mathrm{i}\pi^2 \Gamma_0 \overline{p}_{1,2} + 2L\varepsilon^2 \sigma \overline{p}_{1,1})\rho_f A_f \Gamma_1 L^2 \ln(\alpha_E)\big)\big/(3L^3 \ln(\alpha_E))\overline{A}_1(T_2)\mathrm{e}^{\mathrm{i}\sigma T_2}\overline{A}_1(T_2)\mathrm{e}^{\mathrm{i}\sigma T_2}$$
$$+ \Big(\frac{16\mathrm{i}\omega_1 L\rho_0 A_p p_{1,1}(\alpha_\rho - 1) - 24\pi^2 \rho_f A_f \Gamma_0 p_{1,1}}{9\pi^2} - \mathrm{i}\omega_1 L p_{1,2}\Big(\frac{(\alpha_\rho + 1)\rho_0 A_p}{2} + \rho_f A_f\Big)\Big)\mathrm{D}_2 A_1(T_2)$$
$$- \frac{\pi^4 E_0 A_p (\alpha_E - 1)}{2L^3 \ln(\alpha_E)}((p_{1,1}^2 + 12p_{1,2}^2)\overline{p}_{1,2} + 2\overline{p}_{1,1}p_{1,1}p_{1,2})\overline{A}_1(T_2)A_1(T_2)^2$$
$$+ \frac{\mathrm{i}\omega_1 \mu\pi^2}{L^3}\Big(\frac{32I_p}{9}\Big(p_{1,1}(\alpha_E - 1) - \frac{9\pi^2 p_{1,2}(\alpha_E + 1)}{8}\Big)$$
$$- \frac{\pi^2 A_p (\alpha_E - 1)\big(\big(\frac{B_1^2}{2} + 6B_2^2\big)p_{1,2} + B_1 B_2 p_{1,1}\big)}{\ln(\alpha_E)}\Big)A_1(T_2)$$
$$- \frac{\pi^4 E_0 A_p (\alpha_E - 1)((B_1 p_{1,2} + B_2 p_{1,1})s_{3,1}(T_2) + (B_1 p_{1,1} + 12B_2 p_{1,2})s_{3,2}(T_2))}{L^3 \ln(\alpha_E)}A_1(T_2)$$
$$- \frac{\pi^4 E_0 A_p (\alpha_E - 1)(s_{1,1}(T_2)(B_1 \overline{p}_{1,2} + B_2 \overline{p}_{1,1}) + s_{1,2}(T_2)(B_1 \overline{p}_{1,1} + 12B_2 \overline{p}_{1,2}))}{L^3 \ln(\alpha_E)}\overline{A}_1(T_2). \tag{A7}$$

Appendix B

The transverse displacement in the governing equation (9) is divided into nodes, and the spatial derivative with respect to x can be expressed as follows:

$$v^{[k]}(x_i) = \sum_{j=1}^{N} \varphi_j^{[k]}(x_i)v(x_j) + \Psi_1^{[k]}(x_i)v^{[1]}(x_1) + \Psi_N^{[k]}(x_i)v^{[1]}(x_N), \quad i = 1, 2, \cdots, N, \tag{B1}$$

where $v^{[1]}(x_1)$ and $v^{[1]}(x_N)$ are new generalized variables, and

$$\Psi_j^{[k]}(x_i) = \frac{1}{x_j - x_{N-j+1}}(l_j^{[k]}(x_i)(x_i - x_1)(x_i - x_N) + kl_j^{[k-1]}(x_i)((x_i - x_1) + (x_i - x_N))$$
$$+ k(k-1)l_j^{[k-2]}(x_i)), j = 1, N, \quad i = 1, 2, \cdots, N, \tag{B2}$$

$$\varphi_j^{[k]}(x_i) = \frac{1}{x_j - x_{N-j+1}}(l_j^{[k]}(x_i)(x_j - x_{N-j+1}) + kl_j^{[k-1]}(x_i))$$
$$- \left(l_j'(x_j) + \frac{1}{x_j - x_{N-j+1}}\right)\Psi_j^{[k]}(x_i), \quad j = 1, N, \quad i = 1, 2, \cdots, N, \tag{B3}$$

$$\varphi_j^{[k]}(x_i) = \frac{1}{(x_j - x_1)(x_j - x_N)}(l_j^{[k]}(x_i)(x_i - x_1)(x_i - x_N) + kl_j^{[k-1]}(x_i)((x_i - x_1) + (x_i - x_N))$$
$$+ k(k-1)l_j^{[k-2]}(x_i)), \quad j = 2, 3, \cdots, N-1, \quad i = 1, 2, \cdots, N, \tag{B4}$$

in which N is the number of nodes, k is the order of the weight coefficient of each operator, and $l_j(x)$ is the Lagrange interpolation formula satisfying

$$l_j(x) = \prod_{\substack{k=1 \\ k \neq j}}^{N} \frac{x - x_k}{x_j - x_k}, \tag{B5}$$

$$l_j^{[1]}(x_i) = \begin{cases} \dfrac{1}{x_i - x_j} \displaystyle\prod_{\substack{m=1 \\ m \neq i,j}}^{N} \dfrac{x_i - x_m}{x_j - x_m}, & i \neq j, \\ \displaystyle\sum_{\substack{m=1 \\ m \neq i,j}}^{N} \dfrac{1}{x_i - x_m}, & i = j, \end{cases} \tag{B6}$$

$$l_j^{[k]}(x_i) = \begin{cases} k\left(l_j^{[1]}(x_i)l_i^{[k-1]}(x_i) - \dfrac{l_j^{[k-1]}(x_i)}{x_i - x_j}\right), & i \neq j, \\ \displaystyle\sum_{m=1}^{N} l_j^{[1]}(x_m)l_m^{[k-1]}(x_j), & i = j. \end{cases} \tag{B7}$$

Since the governing equation (9) contains integral terms, it is advisable to integrate the integral quadrature method (IQM) with the DQEM for improved accuracy. Following the IQM principles, an interpolation relationship exists between the node function value and the integral operator as follows:

$$\int_{x_i}^{x_j} f(x,t)\mathrm{d}x = \sum_{k=1}^{N} c_k^{ij} f(x_k, t) \tag{B8}$$

where $c_k^{ij} = A_{jk}^{-1} - A_{ik}^{-1}$.

The elements in the coefficient matrix A are calculated by

$$a_{ij} = \begin{cases} \dfrac{x_i - r}{x_j - r}l_{ij}^{[1]}, & i \neq j, \\ l_{ii}^{[1]} + \dfrac{1}{x_i - r}, & i = j, \end{cases} \tag{B9}$$

where r represents a constant. The existing reference [50] shows that when the constant satisfies $|r| \leqslant 0.1$, the influence of the constant term on the accuracy of numerical simulation can be ignored. To ensure the calculation accuracy, the constant is set to 0.01.